Mechanical modeling of pre-eruptive magma propagation scenarios at calderas

L. Mantiloni [1,2], E. Rivalta [1,3], T. Davis [4]

[1]GFZ German Research Centre for Geosciences, Section 2.1 'Physics of Earthquakes and Volcanoes', Telegrafenberg, 14473 Potsdam, Germany.
[2]University of Potsdam, Potsdam, Germany
[3]Department of Physics and Astronomy, Alma Mater Studiorum University of Bologna, V.le Berti Pichat 8, 40126 Bologna, Italy
[4]University of Oxford, Oxford, United Kingdom

Key Points:

- We present numerical models of crustal stress state at calderas
- We develop a fast dike propagation model and validate it on a previous numerical model
- We combine our stress and dike models to simulate magma pathways at synthetic calderas

Corresponding author: Lorenzo Mantiloni, `lorenzo@gfz-potsdam.de`

Abstract

Simulating magma propagation pathways requires both a well-calibrated model for the stress state of the volcano and models for dike advance within such a stress field. With the purpose of establishing a framework for calculating computationally efficient and flexible shallow magma propagation scenarios, we develop three-dimensional models for the stress state of volcanoes with complex topographies and edifice histories as well as a new simplified three-dimensional model of dike propagation using the stress state of the volcano as input. Next, we combine all these models to calculate shallow dike propagation scenarios for complex caldera settings. The resulting synthetic magma pathways and eruptive vent locations broadly reproduce the variability observed in natural calderas.

Plain Language Summary

Understanding the pathways that bring magma from an underground chamber to the surface helps us preparing for future eruptions in volcanic areas. Dikes are fractures filled with magma and represent the most common mechanism of magma transport in the Earth's crust. Their trajectories may be curved if the Earth's crust is deformed by the load of topography or by tectonic forces. Here we first discuss a model of such deformation processes in volcanic regions with complex but mild topography. Then, we develop a simplified dike propagation model that we validate with a more sophisticated one. Next, we combine our models and simulate magma pathways in artificially-generated scenarios.

1 Introduction

Geophysical observations of ground deformation and seismicity in volcanic areas have highlighted how some eruptions are preceded by a long phase of magma propagation in the form of magma-filled dikes (Einarsson et al., 1980; Ebinger et al., 2010; Nakada et al., 2005; Uhira et al., 2005; Wright et al., 2012; Sigmundsson et al., 2015; Patrick et al., 2020; Cesca et al., 2020; Davis et al., 2021; Smittarello et al., 2022). Some recent dikes have propagated for over 70 km, reaching locations that had not experienced any fissure opening in decades or centuries; in some cases the ensuing lava flows have resulted in massive property damage (Patrick et al., 2020; Martí et al., 2022) or, in the extreme case of the 2021 eruption at Niyragongo, in hundreds of victims (Smittarello et al., 2022). The associated dike trajectories have also displayed a variety of geometries and spatial orientations, from horizontal to oblique to vertical, and shapes, from planar to segmented, curved or twisted (Branca et al., 2003; Bagnardi et al., 2013; Xu & Jónsson, 2014; Sigmundsson et al., 2015; Patrick et al., 2020; Davis et al., 2021; Dumont et al., 2022; Smittarello et al., 2022; Martí et al., 2022). In spite of the importance of this process, there are still no models to forecast, in three dimensions, the trajectory taken by magma during propagation in the shallow crust.

Our physical understanding and our models of dike trajectories have progressed significantly in the last decades. Both early (Anderson, 1937) and more recent works (Dahm, 2000a) have established that dike pathways are largely determined by the balance between the elastic stresses in the host rock and the buoyancy force resulting from the density contrast between magma and rock. As a rule of thumb, dikes open against the direction of the least-compressive principal stress axis (Ziv et al., 2000; Gudmundsson, 2002; Pollard et al., 2005); together with the external stresses, the buoyancy force determines the direction of propagation along the dike tip line (Weertman, 1971; Pollard, 1987; Rubin, 1995; Taisne et al., 2011; Rivalta et al., 2015; Townsend et al., 2017). The simplest 2D trajectories are streamlines perpendicular to the least-compressive stress axis (Anderson, 1937; Pollard, 1987), while the most sophisticated approaches model dikes as cracks steered in the direction of maximum strain energy release rate (Dahm, 2000a; Maccaferri et al., 2010, 2011). Dike trajectory models have recently evolved from two dimensional (2D)

(Anderson, 1937; O. H. Muller & Pollard, 1977; Pollard, 1987; Dahm, 2000a) to partially (Sigmundsson et al., 2015; Heimisson et al., 2015; Pansino et al., 2022), and, finally, fully three-dimensional (3D) by (Davis et al., 2020, 2021). The latter model extends to 3D the maximum strain energy release rate trajectory calculation approach introduced by Dahm (2000a); a 3D equivalent of the simple 2D streamline approaches is still missing.

The 3D model by Davis et al. (2020, 2021) has been applied to explain the counterintuitive trajectory of the 2018 dike at Sierra Negra, Galápagos. Importantly, Davis et al. (2021) confirmed the pivotal importance of a well-calibrated stress field in modelling dike trajectories: contributions from different stress-generating mechanisms, such as topographic gravitational loading and regional stress field, needed to be carefully adjusted in order to steer the dike on the observed trajectory. If we want to simulate 3D dike propagation at arbitrary volcanoes, we also need to determine their state of stress.

This problem was addressed by Rivalta et al. (2019), who suggested a stress inversion strategy which involves, first, establishing the relevant sources of stress for the specific volcano, and then, tuning their relative intensity so that simulated dikes starting from the known location of magma storage reach the known locations of past eruptive vents. This strategy was tested on Campi Flegrei caldera in Italy, using only 2D (plane strain) stress models and 2D streamlines for dike propagation.

Extending the stress calibration strategy by Rivalta et al. (2019) to 3D would pave the way to forecast dike pathways in 3D at any arbitrary volcano. A preliminary step is to set up 3D stress and dike trajectory models that are computationally efficient for the large number of simulations needed by the stress calibration procedure. In this study, we first develop computationally efficient 3D stress field calculations for scenarios with topographic reliefs. Then, we develop a fast, semi-analytical 3D dike propagation model that approximates the sophisticated model by Davis et al. (2020, 2021) but retains the simplicity of 2D streamlines and can also backtrack a dike trajectory from eruptive vent to magma chamber. Finally, we show how to integrate all these models to produce realistic pre-eruptive magma propagation scenarios. We focus on calderas, setting up synthetic topographies inspired by natural systems.

2 Method formulation

We now separately introduce our 3D stress and dike propagation models, and then describe how to combine them in dike propagation scenarios. We use the scenarios to calibrate some needed parameters and validate our propagation method. Finally, we run the propagation model for a set of increasingly complex settings. We assume a homogeneous, isotropic and linearly elastic medium as the host rock, described by rock density ρ_r, Young's modulus E and Poisson's ratio ν. g is the acceleration due to gravity. Symbols and parameters are defined in Table 2.

2.1 Modular model for the state of stress

We describe the state of stress within the host rock by a stress tensor σ_{ij}. Tensional stresses are positive. σ_{ij} is diagonalized to retrieve magnitudes, σ_1, σ_2, σ_3, from most compressive to least compressive, respectively, and eigenvectors, $\vec{v_1}$, $\vec{v_2}$, $\vec{v_3}$, which identify the orientations of the principal stress axes.

We build our 3D stress model following the first-order linear approach by Rivalta et al. (2019), who expressed the elastic stress field σ_{ij} of a volcanic region as the superposition of perturbations from a background stress state σ^0_{ij}, each stemming from a different stress-generating mechanism, according to a first-order linear approach that neglects coupling between the stress sources. We model the stress state of calderas limiting our analysis to tectonic stresses and gravitational loading/unloading because, as dis-

cussed by Rivalta et al. (2019), dike patterns can often be explained by a combination of the two mechanisms, which are in most cases the dominant ones (Gudmundsson, 1995; Roman & Jaupart, 2014; Corbi et al., 2015; Heimisson et al., 2015; Maccaferri et al., 2017; Neri et al., 2018). We do not include contributions associated to pressurized magma reservoirs, intrusions or strains induced by large earthquakes. This has the advantage of limiting the number of parameters in the model, while retaining the stress mechanisms with the largest influence. More contributions can be easily added, if needed in specific cases.

We write the stress tensor at any point in the crust as:

$$\sigma_{ij}(x,y,z) - \sigma^0_{ij}(z) = \sigma^T_{ij} + \sigma^G_{ij}(x,y,z) \tag{1}$$

where the stress terms on the right side arise, respectively, from the regional tectonic stress (T) and the gravitational loading/unloading (G).

The first step in the stress modelling is to define the unperturbed state of stress, σ^0_{ij}, before any of the sources on the right hand side of Equation 1 became active. There are two main assumptions in literature: a laterally-confined medium, that is, no lateral strain can be produced after gravity is turned on (e.g. Martel & Muller, 2000; Savage et al., 1985), resulting in a vertical $\vec{v}_1$:

$$\sigma^0_{xx} = \frac{\nu}{(1-\nu)}\rho_r g z, \quad \sigma^0_{yy} = \frac{\nu}{(1-\nu)}\rho_r g z, \quad \sigma^0_{zz} = \rho_r g z. \tag{2}$$

or a lithostatic stress state:

$$\sigma^0_{xx} = \sigma^0_{yy} = \sigma^0_{zz} = \rho_r g z. \tag{3}$$

Field measurements of subsurface stress (Jaeger et al., 2007) lie somewhat in between those two assumptions. Therefore, σ^0_{ij} can be written as:

$$\sigma^0_{xx} = \sigma^0_{yy} = k\rho_r g z, \quad \sigma^0_{zz} = \rho_r g z, \tag{4}$$

where $k \in [\frac{\nu}{(1-\nu)}, 1]$ (Jaeger et al., 2007; J. R. Muller et al., 2001; Slim et al., 2015). In this study, we always set $k = 1$ and assume a lithostatic unperturbed stress.

The second step is to superimpose the tectonic stress, expressed in terms of three independent components σ^T_{xx}, σ^T_{yy}, σ^T_{xy}, which we assume are uniform (e.g. McKenzie, 1978; Müller et al., 1992).

The third step is to consider gravitational stresses associated to surface loading or unloading. This has often been modeled by distributions of normal forces onto a half-space: they can be applied to both 2D and 3D problems (Dahm, 2000b; Maccaferri et al., 2014; Neri et al., 2018), but are inaccurate near the topography, and provide no information on the stress within the topography itself (McTigue & Mei, 1981). More sophisticated analytical solutions exist, but are either 2D (Savage et al., 1985; McTigue & Mei, 1981) or only for simple topographies (McTigue & Mei, 1987).

Martel and Muller (2000) and Slim et al. (2015) described how to implement topographic loads within Boundary Element (BE) models, where the topography is discretized into a mesh of dislocations. Martel and Muller (2000) considered the effect of topographic loading as akin to cutting an infinite body subject to gravity in two halves along a surface defined by the topography. The gravitational stress imposed by the upper half onto the lower one is then subtracted from the background stress of the body (Martel & Muller, 2000, Figure 3). In practice, this is achieved through imposing boundary conditions on the BEs, depending on the coordinate z of their midpoints and the rock density, which control the overburden or excavation pressure imposed by the topography.

One important point in models such as Martel and Muller (2000) is that the boundary conditions at the BEs representing the topography are univocally fixed only once the

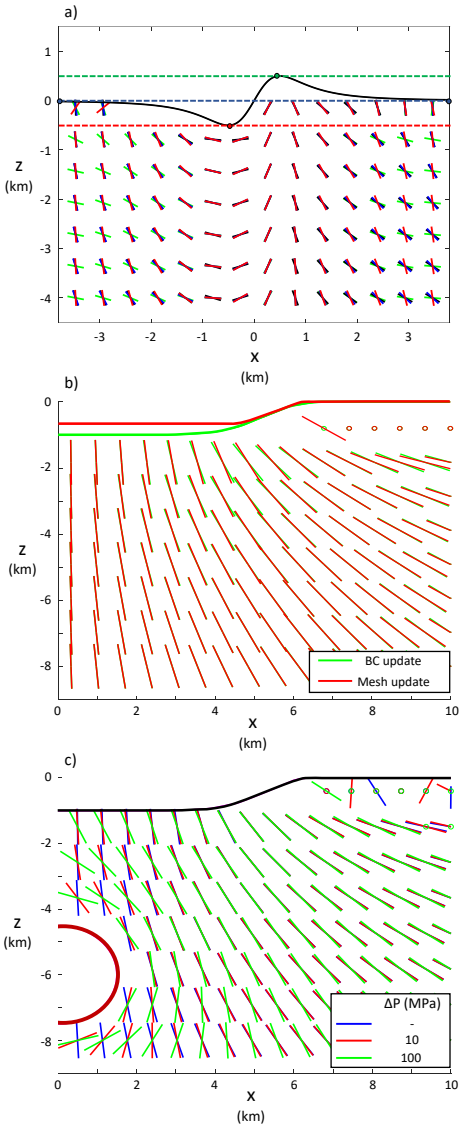

Figure 1. a) Datum level choice: most compressive principal stress orientation due to gravitational loading/unloading of a valley adjacent to a ridge (profile is drawn in black) under plane strain condition. The analytical solution by McTigue and Mei (1981) (black) is compared to our numerical solution with datum level fixed at the flat extremes of the topography (blue), the ridge summit (green) and the valley bottom (red). b) Evolving topography: a 1-km-deep axisymmetric caldera is refilled by 1/3 of its original depth. Least compressive principal stress orientation for two models. Green: the mesh reproduces the caldera before the refilling, and boundary conditions (BC) on the BEs account for the latter. Red: the mesh reproduces the caldera after the refilling. c) Importance of reservoir: least compressive principal stress orientation for three models involving a 1-km-deep axisymmetric caldera and no tectonic stress. Two models include a 6-km-deep spherical magma reservoir of 1.5 km radius, with overpressures ΔP=10 MPa (red) and 100 MPa (green) respectively; one has no reservoir (blue).

datum level, that is the unperturbed surface before any topography is created, is set. This is rarely clarified in applications of similar models (e.g. Chadwick & Dieterich, 1995; Urbani et al., 2017; Neri et al., 2018). Identifying such surface is not always trivial but critical, as different choices lead to different outcomes for the displacement and stress field. We show this in Figure 1a, where we compare $\vec{v_1}$ from the analytical solution by McTigue and Mei (1981) for a valley adjacent to a ridge under plane strain assumption to 2D numerical models where the datum level is set to, successively, the flat extremes of the profile, the ridge summit and the valley bottom. The first model shares the same assumption on the datum level with the analytical solution, hence the good agreement for that case. Such assumption is straightforward to adopt when the topography becomes uniformly flat away from the loaded/unloaded region. However, this is not always the case, and the optimal choice of datum level may depend on the situation. Take e.g. a caldera lying on a coastline, which divides two regions, the mainland and the sea floor, at different elevations. We consider a similar case in our synthetic scenarios, and we solve the ambiguity in the datum level by setting it to the ground elevation before the caldera was formed: this coincides with the sea level in our case. If, for instance, we were to study the formation of an edifice and, later, of a caldera at its summit, we would first set the edifice datum level at its base, and then set the caldera datum level at the edifice summit. Consequently, the topography preceding the reference event (in our scenarios, the caldera formation) informs the datum level.

A further issue regarding the calculation of surface loading/unloading stresses is that they are not immutable. Volcanic regions host a variety of stress-generating and stress-relieving mechanisms acting on different time scales (e.g. McGarr & Gay, 1978; Stephansson, 1988; Savage et al., 1992; Chadwick & Dieterich, 1995). For example, the build-up of a volcanic edifice consists of progressive accumulation of eruptive material that loads and stresses the underlying crust, while, at the same time, magmatic intrusions, earthquakes and inelastic processes tend to relax shear stresses and homogenize principal stresses. Here we avoid this issue by focusing on calderas that we assume have formed relatively recently in the history of the volcano topography, and consider otherwise only mild topographies, so that modeling dike propagation within edifices is not necessary. We elaborate further on this point in Section 4.

We compute $\sigma_{ij}^{G}(x, y, z)$ in Equation 1 following Martel and Muller (2000); Slim et al. (2015). We employ the 3D BE tool *Cut&Displace* (Davis et al., 2017, 2019), based on the displacement discontinuity method by Crouch et al. (1983). The topography is discretized into a mesh of triangular dislocations (Nikkhoo & Walter, 2015), acting as BEs. The 3D mesh needs to be larger than the region of interest, so that its edges are distant enough from the volume where we compute the stress. We find that a mesh with a diameter three times the lateral extent of the studied region is enough for that purpose. If a coastline is present, the outer mesh tapers to two horizontal surfaces at different height, representing the far-field mainland and the far-field sea floor. Once the datum level is fixed, stress boundary conditions are imposed on each BE as we previously described. The load imposed by the water column on the bathymetry is also included.

Calderas are usually filled with eruptive material or sediments over time (e.g. Orsi et al., 1996; Hildreth et al., 2017). Our model can account for this in several ways: the buried caldera floor may be meshed as the reference topographic relief, and corresponding BEs may be loaded accounting for the density contrast between the deeper host rock and the layers above. Alternatively, the current caldera topography may be meshed as the reference topographic relief, and the unloading pressure resulting from the missing mass due to lower density infill is factored in the boundary conditions. Calculations for these options for a synthetic caldera (Figure 1c) show good agreement except in the proximity of the caldera rim. Here we follow the former approach in one scenario, as illustrated later.

We remark that some of the stress sources we neglect, such as magma reservoirs, are in principle straightforward to include in our BE model. In order to show the minor relative influence of such sources, we compare in Figure 1b the orientation of $\vec{v}_3$ for three different models: one without and two with a pressurized, spherical magma chamber, with overpressure of 10 MPa and 100 MPa, all involving the same surface unloading and tectonic stress. Only with extremely large overpressures the effects of the pressurization are felt at a distance of up 1 source diameter. This validates in 3D a similar argument by Rivalta et al. (2019) (see their Figure 1).

2.2 Three-dimensional dike propagation model

2.2.1 Simplified Analytical Model (SAM)

Next, we develop a computationally-efficient 3D dike propagation model that provides a 3D equivalent to 2D $\vec{v}_3$-perpendicular streamlines. There is no straightforward method to compute streamlines in 3D, as the direction of $\vec{v}_3$ alone identifies a surface, while the direction of propagation on that surface remains undetermined. Davis et al. (2020, 2021) developed a pointwise, analytical dike trajectory calculator, similar to Sigmundsson et al. (2015) but fully 3D and more comprehensive in terms of factors considered. Its purpose was to justify why an observed dike took a specific direction depending on the magma buoyancy and the external state of stress, and falls short of being a propagation model. Here we simplify that approach and turn it into a self-propelling 3D propagation model that can also backtrack dike trajectories downward from a vent to the magma storage region. We henceforth refer to our model as the 'Simplified Analytical Model' (SAM).

In the analytical model by Davis et al. (2020, 2021), propagation of the tip-line of a dike occurs when the local mode I stress intensity factor, K, is larger than the fracture toughness, K_c, of the host rock (e.g. Secor Jr & Pollard, 1975). The dike is represented as a tensile, penny-shaped crack with a fixed volume, V, and radius, c. It is assumed that external stress varies linearly in every direction over the crack surface, and that internal pressure varies linearly with z proportional to $\rho_m g \sin\beta$, where β is the crack dip. In such case, K can be written as:

$$K = \frac{3\mu V}{4(1-\nu)c^2\sqrt{\pi c}} + \frac{4}{3\pi}(\Delta\gamma c\sqrt{\pi c})\cos\alpha, \tag{5}$$

(Tada et al., 2000), where α is the angle spanning the circumference of the crack away from the direction of the maximum linear pressure gradient loading the dike plane, $\Delta\gamma$. The first term in Equation 5, which depends only on V, determines the magnitude of K. The second contribution, which accounts for the effect of $\Delta\gamma$, determines the angle α for which K is maximum, and thus the direction of propagation of the crack. If $R_K = K/K_c > 1$, the crack is expected to propagate (see Figure 1 in Davis et al., 2020).

In SAM, we simplify such approach by, first, assuming that the dike opens against the local $\vec{v_3}$, calculated from the stress model defined in Section 2.1, and is represented as a penny-shaped crack with fixed radius c. Secondly, we calculate K as

$$K = \frac{4}{3\pi}(\Delta\gamma c\sqrt{\pi c}). \tag{6}$$

This is equivalent to neglecting the role played by the dike volume and K_c in determining whether the dike will advance. On the other hand, the buoyancy force contributes to $\Delta\gamma$ in SAM, and plays a role in determining the direction of propagation on the $\vec{v_3}$-perpendicular surface.

We use a Cartesian reference frame, where the z-axis is positive upward (Figure 2a). We later employ a cylindrical reference frame to identify the starting points of dikes (Figure 2a) where the radial distance from the origin is indicated as r and the angle measured counterclockwise from the positive x-axis is indicated as ϕ.

We calculate forward dike trajectories (FTs) as follows:

1. We produce a stress model for the hosting medium (section 2.1).
2. We choose a starting point F_0 for the dike (for instance, at the edge of a magma reservoir).
3. We compute σ_3 and $\vec{v_3}$ at F_0 and identify the local surface Σ perpendicular to $\vec{v_3}$. The dike is then defined as a penny-shaped crack of radius c lying on Σ (Figure 2a).
4. We compute K along the dike's tip-line. To do so, we generate a ring of n regularly-spaced observation points O_i, $i = 1...n$ at a distance c from F_0 (Figure 2b).
5. We calculate σ_3^i at each O_i and use it in place of the normal stress to calculate $\Delta\gamma$ for every point on the ring as:

$$\Delta\gamma_i = \frac{(\sigma_3^i - \sigma_3^j)}{2c} - \rho_m g \frac{(z_O^i - z_O^j)}{2c}, \tag{7}$$

   where z_O^i, z_O^j are the vertical coordinates of points O_i, O_j, with O_j antipodal to O_i.
6. We calculate K^i at each O_i according to Equation 6 and determine the point F_1 where $K^i = K^{max}$. This will identify the direction of propagation of the dike (Figure 2b).

We reiterate the previous steps taking F_1 as the current F_0. This will produce a chain of points identifying the trajectory of the dike. The dike stops once at least one of the observation points generated in step 3 reaches the free surface. The center of the current Σ is then taken as the arrival point F_A (Figure 2b). In our stress models, however, a further issue emerges. In general, a minimum distance threshold (MDT) needs to be maintained between the observation points and the mesh, in order to prevent artifacts singularities in the stress calculations (Slim et al., 2015). This is a characteristic issue of BE models, and can be mitigated with finer meshing, or aligning the observation points to the midpoints of the BEs (Slim et al., 2015). Due to this issue and to the finite size of the BEs representing the free surface, we do not allow dikes to proceed beyond a certain distance from the free surface. Here we fix the MDT to 800 m away from the nearest BE, as this is the average size of the dislocations of the mesh we employ. Dikes may be propagated past their F_A until they hit the surface at a 'projected' arrival point, F_A^P, assuming that they maintain the dip and strike calculated at F_A (Figure 2b). This is akin to assuming that dikes do not have the space to adjust to the local stress field in the last 1 km before reaching the free surface. A SAM dike is forced to stop if the trajectory becomes horizontal, or if the difference in the strike and dip angles between the current direction of propagation and the one at the previous step is larger than a given threshold. This prevents abrupt turning in the dike pathways.

SAM trajectories depend on two parameters, c and n. We found that values of n equal or greater than 12 lead to nearly identical dike pathways; we set n to 12 in all scenarios calculated later. In contrast, different c lead to different trajectories and arrival points for the same starting points and stress field. Large c (e.g. > 2 km if the dike starting point is 10 km deep) sample the stress field in too few points and do not produce accurate trajectories, while very small c (e.g. < 50 m for the starting depth mentioned above) are computationally expensive and follow principal stress directions nearly pointwise, as streamlines do in 2D. In this perspective, c controls how much SAM trajectories deviate from the stress directions. We show later how c may be calibrated to better match a more sophisticated dike propagation model.

SAM also allows for the propagation of anti-buoyant dikes, that is, dikes filled with $\rho_m > \rho_r$ propagating downward through the crust. Dike trajectories, however, cannot be backtracked by simply inverting the density contrast between magma and rocks: an anti-buoyant dike starting from the arrival point of a buoyant one and propagating downward with the same c and n will not pass through the same points (see Figure 2c), even

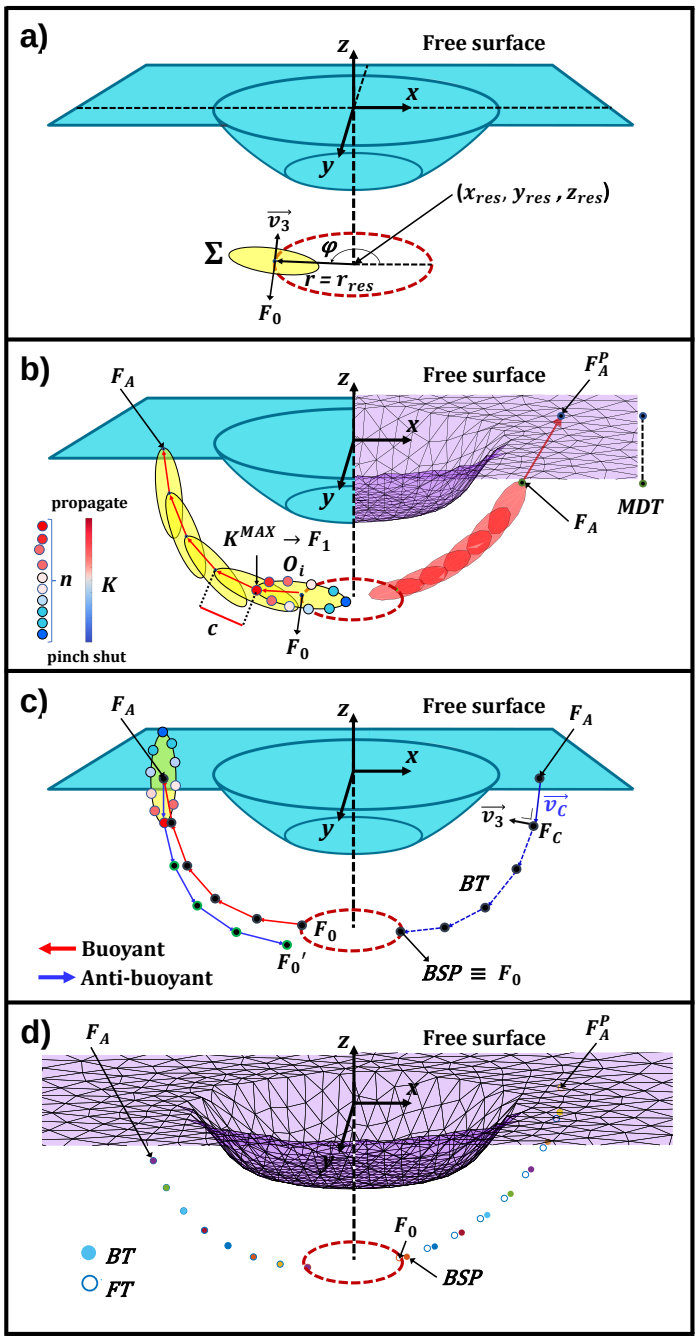

Figure 2. SAM framework. a) reference systems employed throughout the work and notation for the dike radius and starting point. Blue surface: simplified topography with a circular caldera. Red dotted line: edge of a magma storage region where the dike departs. Yellow surface: dike's initial opening surface (Σ). b) Left: full SAM trajectory, arrival point and detail of first step of the algorithm. Colored dots: observation points O_i; the colors are associated to K according to the colorbar. Right: BE mesh of the topography (vertically exaggerated) and actual FT from scenario STC-3 (see Section 2.3), extended until the free surface. Black dotted line on the right: MDT (here set to 2 km). c) Backtracking of SAM trajectories. Left: comparison between buoyant (red) and anti-buoyant (blue) trajectories. Right: representation of the backtracking algorithm outlined in Section 2.2. d) Backtracked trajectories (BTs) of the foward trajectory (FT) shown in b). Left: BT starts from the actual arrival point. Right: BT starts from the projected arrival point. Colored dots on both sides represent the BTs; empty blue dots the original FT.

if, as we observed, the difference between forward trajectories (FTs) and backtracked trajectories (BTs) decreases for smaller values of c.

We backtrack FTs, from known arrival points F_A and with assumed parameters c_B and n_B, as follows:

1. Starting from F_A, we find a candidate point B_C at a distance c_B such that the scalar product between $\vec{v}_3$ at B_C and the vector $\vec{v}_C$ pointing from B_C to F_A is minimal (Figure 2d).
2. We run one step of the forward model from B_C and calculate the vector between the predicted and actual F_A; we then shift B_C by that same vector and iterate this procedure until the desired precision is attained, and B_C is taken as the first point B_1 of the BT.
3. The algorithm stops as soon as a specific requirement is satisfied: for instance, the current B_j falls within the known magma storage region. The lastly-recovered point of the BT becomes then the "backtracked starting point" (BSP) (Figure 2d).

The first step of the algorithm is modified when starting from F_A^P lying on the free surface, as we no longer fix the distance between B_C and F_A^P to a specific c_B, but let it vary over a specific range (for a FT with given c, we find a 0-3c range enough for our purpose).

We tested the method against known forward trajectories, and found that it is able to retrieve each F_0 within a range of a few tens of meters if starting from F_A, and a few hundreds if starting from F_A^P, provided the same radius c of the forward model is employed ($c_B = c$). If that is not the case, the distance between actual and backtracked starting point ($\Delta_{BSP} = |F_0 - BSP|$) increases with the difference between the backtrack radius c_B and c.

2.2.2 Three-dimensional Intrusion Model (TIM)

We later validate SAM against a more sophisticated dike propagation model. To this end, we employ the numerical, full-3D dike propagation model by Davis et al. (2020) and Davis et al. (2021). The model needs the dike volume (V), assumed constant during the propagation, and the magma density (ρ_m). The dike starts as a penny-shaped crack centered at a specific starting point and arranged according to a starting dip and strike; these can be either arbitrary or coincide with the local $\vec{v}_3$. The dike starting radius is then taken as $c_0 = \sqrt{V/1.6\pi}$. The dike is discretized into a mesh of triangular dislocations, and R_K is computed at every BE lying on the dike tip-line (Davis et al., 2019); the tip line is advanced or retreated by an amount proportional to the local R_K, depending on its sign, and the crack is remeshed. The crack can also bend out of its plane according to the maximum circumferential stress criterion (Pollard et al., 2005; Davis et al., 2021). The dike can thus advance along complex trajectories and change its shape in the process. As such, the model captures the effect of dike volume and buoyancy as well as the external stress. In the following, we refer to it as 'Three-dimensional Intrusion Model' (TIM).

Before comparing TIM and SAM trajectories, we illustrate how to combine the stress and dike models introduced so far into synthetic scenarios of dike propagation.

2.3 Setup of dike propagation scenarios

We start by producing a stress model for a given caldera. In a real case, we first evaluate which stress mechanisms are most relevant. Here, as discussed in Section 2.1, we limit our analysis to tectonic stresses and gravitational loading/unloading. We calculate the latter as described in Section 2.1, and we superimpose to the resulting stress field the tectonic stress components σ_{ij}^T.

Table 1. Parameters of the dike propagation model.

Symbol	Description	Units
Host rock density	ρ_r	kg/m^3
Magma density	ρ_m	kg/m^3
Host rock fracture toughness	K_C	Pa$\sqrt{\text{m}}$
Young's modulus	E	Pa
Poisson's ratio	ν	
Forward dike trajectory	FT	
Dike starting point	F_0	
Dike radius	c	m
Dike surface	Σ	
Number of observation points along the dike tip-line	n	
Observation points	O_i, $i = 1,...,n$	
Dike arrival point	F_A	
Points defining dike trajectory	F_i, $i = 1,...,A$-1	
Projected dike arrival point	F_A^P	
Backtracked dike trajectory	BT	
Backtracked dike radius	c_B	m
Points defining backtracked trajectory	B_i	
Backtracked dike starting point	BSP	

We fix the location of the magma reservoir, which will constitute the rock volume where dikes depart from. Dike starting points are described by z_0^k, radius r_0^k and angle ϕ_0^k, $k = 1,...,N$ (Figure 2a). In simplified scenarios, we fix equally-spaced starting points along the edge of circular, sill-like reservoirs. In more complex scenarios, starting points are generated from a probability distribution in z, r, ϕ that quantifies our uncertainty on the favored dike nucleation sites around the reservoir.

As a final step, we choose a model of dike propagation and define the needed input. TIM needs dike volumes (V^k), magma densities (ρ_m^k), K_c of the host rock and a starting geometry for the k-th dike. Starting dike radii are fixed as $c_0^k = \sqrt{V^k/1.6\pi}$ (see Section 2.2 and Davis et al., 2021). SAM needs c and ρ_m: here, they are the same for all dikes in each scenario.

We produce a total of eight synthetic scenarios, referred to as STC-i, $i = 1, ..., 8$ (Tables 2 and 3). We fix the Young's modulus and Poisson's ratio of the medium to $E =$ 15 GPa and $\nu = 0.25$, respectively. The fracture toughness of the host rock is fixed to $K_C = 70$ MPa·m$^{1/2}$. The densities of the host rock (ρ_r) and the magma filling the dikes (ρ_m) are set as in Tables 2 and 3.

We consider increasingly complex topographies with an approximately circular or elliptic caldera located at the origin of the cartesian reference frame (see Figure 2a). A resurgent dome may also be included, as well as a coastline and/or hills. We employ four main topographic settings, each corresponding to one or more scenarios:

1. Setting 1 (STC-1,3): a flat topography with a circular caldera of radius $R_C = 6$ km and maximum depth $d = 500$ m. The depth of the caldera, which has steep slopes and a flat floor, varies with r according to:

$$z = \exp\left(-r^6\right) \tag{8}$$

2. Setting 2 (STC-4,5): we add a coastline to the flat topography from (1), modelled as a steep elevation step along the y-axis. The bathymetry lies 100 m below the datum level. The caldera has $R_C = 6$ km, $d = 450$ m, and depth varying with r as in (1).
3. Setting 3 (STC-2,6,7): we maintain the bathymetry of (2), but we include two hills (heights 791 m and 355 m, base diameter ∼15 km). The caldera has $R_C = 6$ km and maximum depth $d = 424$ m. The caldera shape is made irregular by adding Gaussian noise to Equation 8. In STC-6 we model a topography evolving from setting (3) to (3b), where the caldera is partially refilled, with its maximum depth changing to $d = 221$ m.
4. Setting 4 (STC-8): an elliptic caldera with $d = 150$ m, semi-major and semi-minor axes $a_C = 8$ km and $b_C = 4$ km, respectively. A circular resurgent dome with $h = 150$ m and 4.8 km diameter is located 3 km offset from the caldera center. The external topography has some gently-sloping hills (the maximum height is 157 m), but no bathymetry.

All scenarios involve tensional stresses, whose principal axes coincide with the coordinate axes except for STC-5.

For all scenarios except for STC-2,7,8 dikes nucleate at same depth $z_0^k = z^{\text{res}}$ and radius $r_0^k = r^{\text{res}}$ (see Table 3 for numerical values). In STC-2, we include a starting point at a radius larger than r^{res}. Two different nucleation depths and radii are considered in STC-7. In STC-8, z_0^k are drawn from a beta distribution skewed towards the upper edge of the reservoir (see Figure 5f). STC-1 has only one starting point. ϕ_0^k are equally-spaced in STC-2,3,4,5 and drawn from a uniform distribution in STC-7,8. All nucleation volumes are centered at the origin of the cartesian reference frame, except for STC-8, which is centered below the summit of the resurgent dome. We remark that here these 'reservoirs' where dikes depart from have no contribution to the stress field.

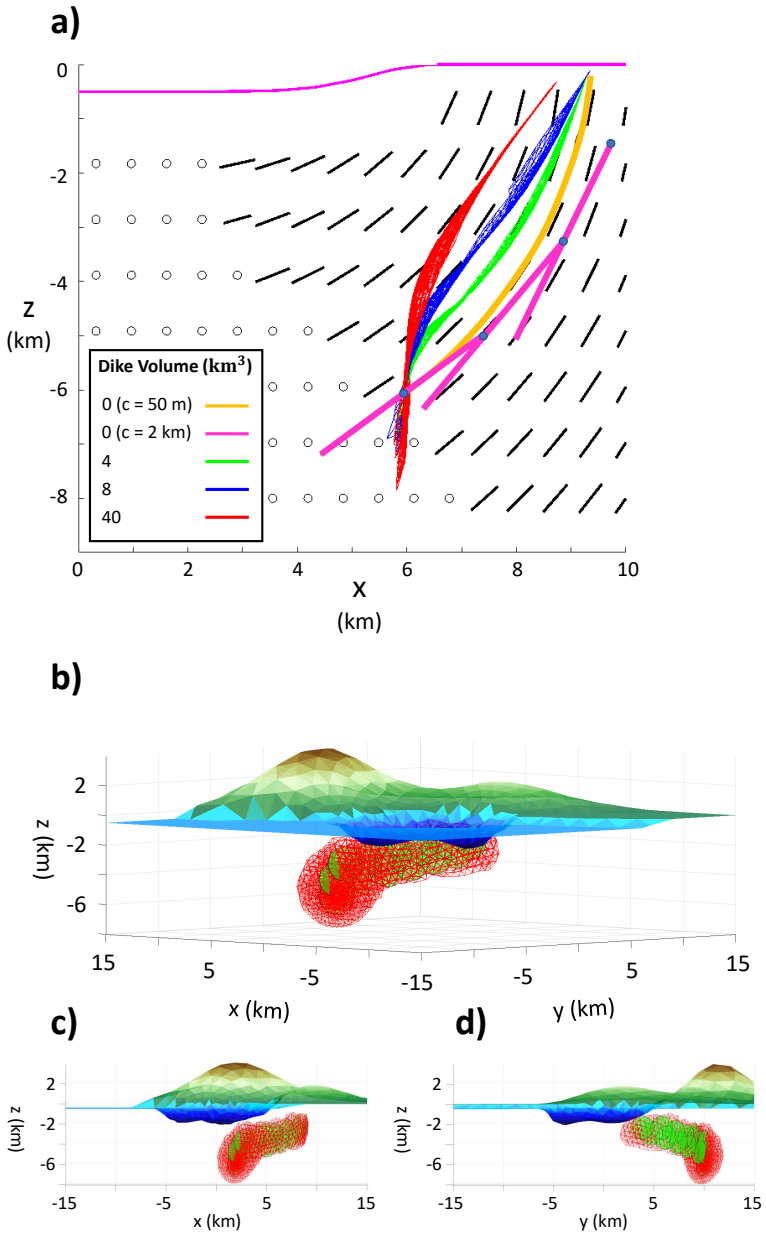

Figure 3. TIM and SAM comparison. TIM pathways: series of meshes representing a subset of steps in dike propagation. Starting and final configuration of dikes are always included. Triangular dislocations are shown as red, empty triangles. a) In scenario STC-1, two SAM dikes with different c compared to to three TIM dikes with the same magma density and increasingly larger volumes. All dikes start from $x = 6$ km, $y = 0$ km, $z = -6$ km; dikes are vertically-oriented at the starting point. Black segments show $\vec{v}_1$ projected over the x-z plane; black circles represent out-of-plane $\vec{v}_1$. Topography is represented as a magenta line. Blue dots mark the actual trajectory of SAM dike with largest c. b) In scenario STC-2, perspective view of first TIM dike and associated SAM dike propagating laterally beneath a topographic high. Both dikes start from ($x = 2$ km, $y = 10$ km, $z = -6$ km), aligned to local $\vec{v}_3$. c) Side view of b) along x-axis. d) Side view of b) along y-axis. For host rock and magma properties see Table 2.

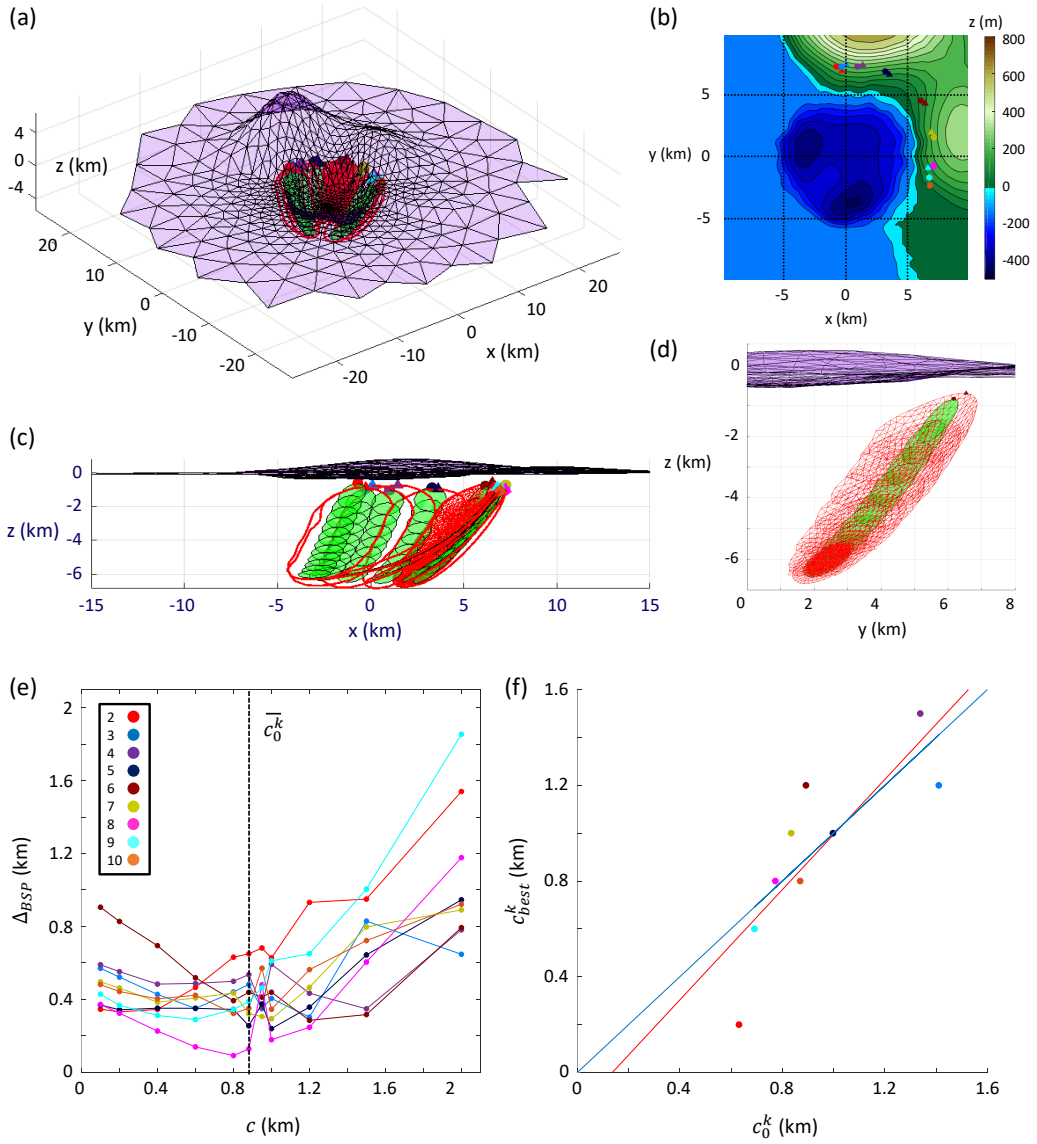

Figure 4. STC-2 scenario: TIM and SAM comparison. Only outlines of TIM pathways are shown, except for the fifth dike, shown as a series of steps in the simulation as in Figure 3. a) synthetic topography with a vertical exaggeration factor of 10. b) elevation map and arrival points of TIM (triangles) and SAM (dots) dikes. Each dike is associated to a fixed color. c) side view of topography, TIM (red) and SAM (green) pathways, dike starting and arrival points. TIM pathways are outlined except for the fifth dike, where we display the BE mesh. d) detail of TIM and SAM pathways for the fifth dike. Triangular dislocations in TIM are visible as red, empty triangles. e) SAM backtracking method applied to TIM pathways; distance between the actual and backtracked starting point Δ_{BSP} versus c. Black dotted line marks the average of c_0^k of TIM dikes. Colors correspond to dikes as in b) and c), and are associated in the inset to STC-2 dikes in Table 2. f) c_{best}^k: c yielding the smallest Δ_{BSP} versus starting dike radius for each dike. The red line fitting the data is compared to the bisector (blue line).

Table 2. Parameters of TIM dikes in STC-1 and STC-2.

Dike	V_k $\cdot 10^6$ m^3	c_0^k km	ρ_m^k kg/m^3
STC-1			
1	4	0.89	2300
2	8	1.26	2300
3	40	2.82	2300
STC-2			
1	4	0.89	2700
2	2	0.63	2300
3	10	1.41	2250
4	9	1.34	2100
5	5	0.99	2280
6	4	0.89	2350
7	3.5	0.83	2300
8	3	0.77	2270
9	3.8	0.87	2390
10	2.4	0.69	2300

2.4 SAM and TIM comparison

We now proceed to validate SAM against TIM to assess under which conditions the two models are compatible and, in particular, how a proper calibration of c allows SAM to match TIM pathways, both in forward and in backward. In particular, we want to test the hypothesis that the c leading to the best match between SAM and TIM dikes may coincide with their starting radius ($c = c_0$) or, if multiple TIM dikes are present, the average of their starting radii ($c = \bar{c}_0^k$).

We use STC-1, which offers the simplest topography, and STC-2, which offers the most complex one, to compare TIM and SAM and to calibrate c. For TIM dikes, we fix volumes (V^k), starting radii (c_0^k) and magma densities (ρ_m^k) as in Table 2. In STC-1 (Figure 3a), we show a situation where the two models diverge. We run three TIM dikes with different V^k and two SAM dikes with different c, propagating from the same starting point and with the same ρ_m. While TIM dikes start with an arbitrary, vertical orientation, SAM dikes have to start perpendicular to $\vec{v_3}$. This leads to very different pathways between SAM dikes and TIM dikes. From Figure 3a, it is evident how TIM dikes with larger volumes require larger distances to adjust to the stress directions, as already captured in 2D models (Dahm, 2000a; Maccaferri et al., 2010). We also notice how the SAM dike with the smallest c follow the stress field more closely. Thus, SAM and TIM dikes converge to the same trajectory only if the latter start already oriented to the external stress or, alternatively, if SAM dikes start where TIM ones have adjusted to it.

In STC-2 we show a situation where SAM dikes capture 3D propagation as well as TIM dikes. In Figure 3b,c,d, we run a TIM dike starting beneath a topographic high, and compare it to a SAM dike starting from the same point. In this model, we set both dikes to be weakly buoyant ($\rho_r - \rho_m = 100$ kg/m^3) and start already aligned to the local stress directions. They both propagate laterally along similar trajectories, as dictated by the external stress and the low magma buoyancy: such behavior may not be captured by 2D dike models. We find that the SAM dike fits the TIM pathway best if we take $c = c_0^1$, that is the starting radius of TIM dike (Table 2). In Figure 4a,b,c,d, we run additional nine TIM dikes with different V^k, c_0^k and ρ_m, and compare them to

forward SAM trajectories. Despite the V^k, c_0^k and ρ_m^k being different from one dike to another, the arrival points and final orientations of the SAM dikes are consistent with the outcomes of the TIM dikes, and SAM trajectories follow closely TIM ones. We find that such match is closest when we take $c = \bar{c}_0^k$, that is, the average of the c_0^k.

We also backtrack the nine TIM dikes with SAM, and evaluate how accurately their starting points are recovered with different values of c_B (Figure 4e,f). The BTs start from the TIM arrival points and stop once the lastly-retrieved point goes past z^{res} (here assumed known). We find that the performance of our backtracking method in recovering the SP of the TIM dikes depends on the c we employ. Both large (> 1.2 km) and small (< 0.6 km) c perform poorly. On the other hand, we see in Figure 4e how the distance between actual SP and BSP of each dike, Δ_{BSP}, is smallest for c equal or close to $\bar{c}_0^k = 880$ m (black vertical line in Figure 4e). The minimum of Δ_{BSP} for all dikes except for the one with the smallest V^k (Table 3) is found in the range 600m $\leq$ c $\leq$ 1km.

In Figure 4f, we plot c_0^k versus c_{best}^k, that is, the c leading to the most accurate BSP for the k-th dike. We find that the best-fit line comes close to the bisector of the quadrant and, thus, $c = c_0^k = \sqrt{V^k/1.6\pi}$ provides a good estimate for the optimal c in SAM.

In summary, SAM provides trajectories close to TIM dike trajectories only when the latter are well-oriented within the external stress field. Then, the optimal c for SAM may be chosen on the basis of the volumes of TIM dikes. The implication is that, in a real scenario, knowledge on the volume of actual dikes could inform the choice of c for both forward and backward SAM.

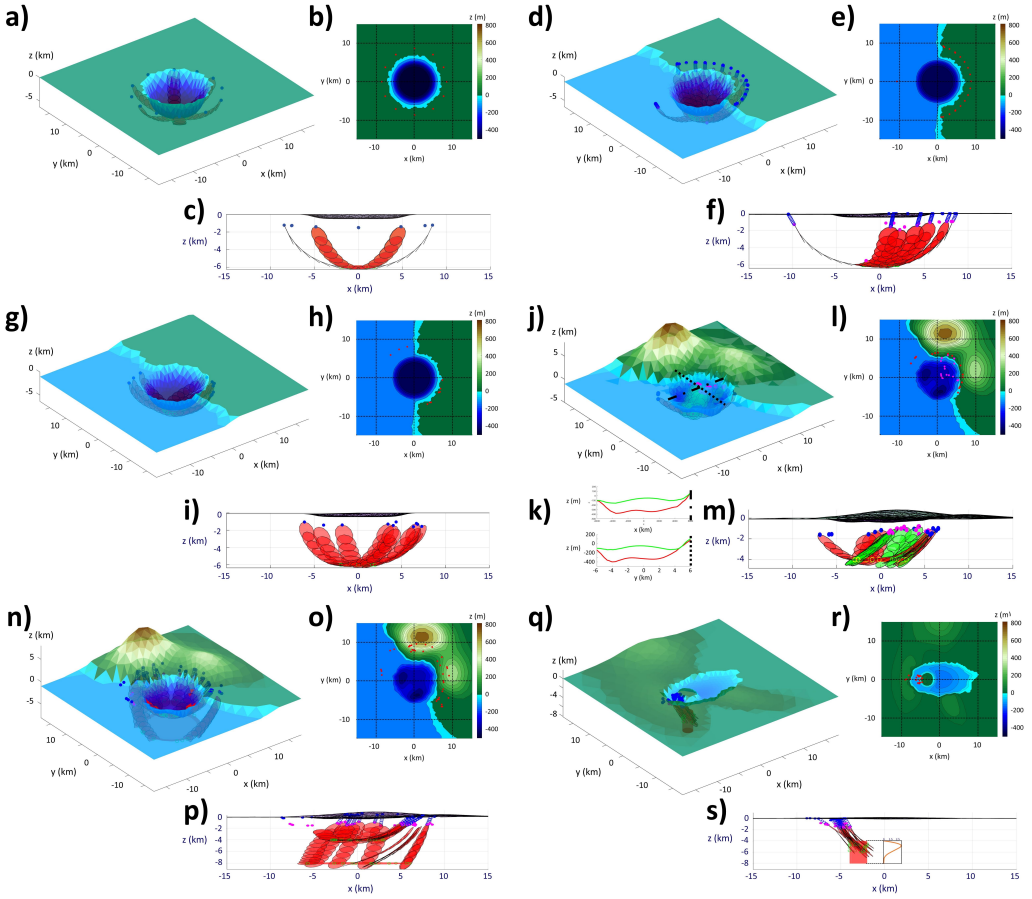

Figure 5. Topography and selected SAM dike trajectories for scenarios STC-3 to STC-8. a), b), c) STC-3: respectively, synthetic topography and dike trajectories, elevation map and dike arrival points, side view of topography and dike trajectories. d), e), f) STC-4: respectively, synthetic topography and dike trajectories, elevation map and dike arrival points, side view of topography and dike trajectories. g), h), i) STC-5: respectively, synthetic topography and dike trajectories, elevation map and dike arrival points, side view of topography and dike trajectories. j), k), l), m) STC-6: respectively, synthetic topography (original and updated) with two cross-sections along x (dots and dashes) and y (fine dots) axes and dike trajectories (red ones run with original topography, green ones with updated topography), topographic profiles along cross-sections in j) showing original (red) and updated (green) topography, elevation map and dike arrival points, side view of topography and dike trajectories. n), o), p) STC-7: respectively, synthetic topography and dike trajectories, elevation map and dike arrival points, side view of topography and dike trajectories. q), r), s) STC-8: respectively, synthetic topography and dike trajectories, elevation map and dike arrival points, side view of topography and dike trajectories with inset showing the probability distribution from which vertical coordinates of dike starting points are drawn. General conventions as follows. Topography in a), d), g), j), n), q) has a vertical exaggeration factor of 10. Dike starting and arrival points are represented as green circles and blue dots (red in elevation maps), respectively. In d), f), n), p), q), s) last points of dike trajectories in subsurface are magenta dots and blue circles are steps of projected dike trajectories to free surface. Magma storage regions: light-red volumes.

Table 3. Chosen topography, tectonic stress, host rock and reservoir parameters of the synthetic scenarios.

# Scen.	d	h	σ_{xx}^T	σ_{yy}^T	σ_{xy}^T	ρ_r	r^{res}	z^{res}
	m	m	MPa	MPa	MPa	kg/m^3	km	km
STC-1	500	-	1	0	0	2500	6	6
STC-2	424	-	1	0.4	0	2800	10.2	6
							3	6
STC-3	500	-	1	0.5	0	2500	2	6
STC-4	450	-	1	1	0	2500	2	6
STC-5	450	-	0.8	0.8	-1	2500	2	6
STC-6	424	-	1	0.4	0	2800	3	4
	221							
STC-7	424	-	1	0.4	0	2800	3	4
							6	8
STC-8	150	150	1	0.6	0	2500	1	6

3 Results

In scenarios STC-3 to STC-8, we use SAM to produce dike pathways and vents (Figure 4). FTs are stopped at the distance threshold from the BEs in STC-3,5,6. Conversely, FTs are propagated past that threshold in STC-4,7,8 according to the method explained in Section REF. STC-4,7,8 are thus the only scenarios where surface vents are produced.

The simplest model is STC-3 (Figure 5a,b,c), where the caldera is an axisymmetric, circular depression on a flat surface. Here, dike trajectories are deflected by the gravitational unloading associated to the caldera, and their arrival points punctuate its rim. The tectonic extension is higher along the x-axis, and this leads to the spacing between neighboring arrival points becoming smaller when closer to that axis, even if the starting points are equally spaced.

STC-4 (Figure 5d,e,f) presents a more complex topography, where a simplified caldera lies on a coastline between two flat regions at different heights. This has an evident impact on dike trajectories, which are still deflected away from the caldera, but end up mostly on the mainland. Only the dike starting farthest away from the mainland manages to reach the sea floor. In particular, there is a concentration of arrival points close to the coastline. The effect of deviatoric tectonic stress is most apparent in STC-5 (Figure 5g,h,i). Here, the least-compressive principal tectonic stress axis roughly strikes along the bisector of the second and fourth quadrants (respectively, negative x-axis and positive y-axis, and viceversa). Arrival points cluster about such axis, both on the mainland and on the sea floor.

STC-6 (Figure 5j,k,l,m) considers two different topographies. The first, associated to the red dike set, is the same as STC-2. Dikes are deflected away from the caldera and punctuate its rim on the mainland. Three dikes reach the sea floor. Topographic loads associated to the hills in the first quadrant also tend to attract dikes. The second topography, associated to the green dike set, envisions a partial refilling of the caldera, with a resurgent dome at its center (see Figure 5k). The topography outside the caldera rim is unchanged. Dikes are still deflected by the caldera unloading and focus towards the mainland, but all reach the surface along or within the caldera rim, some ending up on the resurgent dome. We remark that also in STC-2 both TIM and SAM dikes are deflected toward the mainland and along the rim of the caldera (Figure 4a,b,c,d). Even the

dikes starting from the sea side of the reservoir end up on the mainland. Dikes that propagate in the proximity of the hills are also deflected towards them.

STC-7 (Figure 5n,o,p) shares the topography of STC-2, but includes two different dike nucleation depths and radii. Dike trajectories show the same pattern as in the previous scenario, the ones starting from the deeper nucleation region reaching the surface farther away from the caldera.

Dikes in STC-8 (Figure 5q,r,s) feel the competing influence of the elliptic caldera and the loading due to the resurgent dome and the hill on the left. The synthetic vents cluster in two areas, the larger adjacent to the dome and the minor close to the caldera rim and the hill. No vents are present at the top of the dome.

In summary, topography plays a dominant role in controlling dike pathways in our scenarios. Even short-wavelength topographic features, such as a $\sim$ 5-km-wide resurgent dome in STC-8 (Figure 5r), influence close trajectories over a distance comparable to their width, e.g. the resurgent dome diameter in STC-8. In all scenarios, dikes are consistently deflected away from surface unloading and attracted by surface loading. Tectonic stress also influences dike orientation and clustering of arrival points, with a more evident impact in the simplest scenarios (STC-3,4,5).

4 Discussion

We have shown how our newly-developed 'elementary' dike propagation model (SAM) well reproduces trajectories calculated with a sophisticated numerical model (TIM) by Davis et al. (2020, 2021) (Figures 3b, 4), and can effectively model 3D dike pathways in synthetic calderas with tectonic stress and mild surface loading/unloading (Figure 5). In particular, SAM and TIM trajectories are similar only if dikes in the latter model start optimally-oriented to the external principal stress directions (Figure 3a). Dike propagation in both models is controlled not only by the gradients of external stress, but also by magma buoyancy. SAM is also able to backtrack dike trajectories from a vent to the magma storage region.

Due to our simplifying assumptions, our models have many potential limitations. The assumptions include homogeneous elastic parameters for the host rock. Rigidity and density layering may substantially affect dike propagation. For instance, dike trajectories can be deflected when crossing interfaces between layers with strong rigidity contrasts, as shown in 2D by Maccaferri et al. (2010). Similar studies are needed to grasp the effects of layer interfaces in 3D. As shown by Mantiloni et al. (2021) through analog experiments, homogeneous models well reproduce the observed pathways provided that 'effective' stress parameters are employed, rather than those actually imposed on the gelatin. In this perspective, our simple models will be of advantage in future real-time or statistical applications, where fast computation is required.

We also assume linear elasticity. Volcanic regions are known to host inelastic processes such as seismicity, damage, thermoplasticity, infiltration of and alteration by hydrothermal and magmatic fluids, that can affect both stresses and dike propagation. In particular, these inelastic processes compete with stress-generating mechanisms by homogenizing stresses (e.g. McGarr & Gay, 1978; Stephansson, 1988; Savage et al., 1992). Repeating magmatic intrusions (e.g. Dieterich, 1988; McGuire & Pullen, 1989; Ventura et al., 1999; Walter et al., 2005) may also bring the state of stress to isotropic in the long run: since they tend to open perpendicularly to $\vec{v_3}$, the strain they cause tends to bring σ_3 closer to σ_1(Chadwick & Dieterich, 1995; Bagnardi et al., 2013; Corbi et al., 2015, 2016). Additionally, faulting and earthquakes may dissipate shear stresses over time. Thus, the stress contributions in Equation 1 are not immutable. An accurate calibration of the stress state needs to take into account the relaxation of each stress contribution over time and space, discriminating between stress sources (in particular topography-altering events)

that became active at different times. For instance, Maccaferri et al. (2017) explored the interplay between the loading stress due to the growth of a volcanic edifice, that dissipates over time, and the 'instant' stress change due to flank collapse in controlling eruptive vent patterns, showing how the latter can deflect dike pathways and lead to the formation of new eruptive centers. These processes are difficult to constrain and are currently accounted for through approximations. For instance, some works set the deviatoric stresses arising from gravitational loading of the edifice to zero (Heimisson et al., 2015; Davis et al., 2021), arguing that they would be compensated by faulting and dike intrusions over the history of the volcano. Corbi et al. (2015) found that superposing the effect of caldera unloading to a volcanic edifice where the state of stress is set to isotropic, rather than fully loaded, explained much better the orientation of eruptive fissures at Fernandina, Galapagos. Here we neglected such processes by creating scenarios where dikes propagate below and around a caldera but not within an edifice. We tested that accounting for shear stress dissipation and stress homogenization in such scenarios still leads to dike trajectories being deflected by surface unloading and attracted by surface loading. We postpone the study of scenarios that involve propagation within an edifice to a future study.

As we show in Figure 1c, stress contributions of magma reservoirs are dominant only in the proximity of the stress source. Such effect, nonetheless, can be important in determining nucleation points for dikes (Gudmundsson, 2006; Grosfils et al., 2015), that we do not model precisely here, as well as attracting or repelling incoming dikes if the reservoir pressure is increasing or decreasing, respectively (Pansino & Taisne, 2019).

Stress contributions due to previous large earthquakes may also deviate dikes or arrest their propagation. This has been considered both through theoretical (Maccaferri et al., 2014, 2016) and analog (Le Corvec et al., 2013) modeling. The fault-generated stresses do not influence dike trajectories significantly unless they come to close proximity and, thus, can hardly reproduce observed dike patterns alone (e.g. Maccaferri et al., 2014). However, Maccaferri et al. (2016) showed how a pre-stressed fault can effectively stop dike propagation if a dike hits it at a sub-perpendicular angle. This is due to the stress induced by the approaching dike, which leads to the fault slipping and, in turns, induces compressive stress at the dike's tip, arresting it. Faults and dikes may also interact with each other, for instance alternately accommodating tectonic extension (Gómez-Vasconcelos et al., 2020).

Lastly, the emplacement of dikes affects the local stress field as well, as both analytical (Rubin & Gillard, 1998) and numerical models (Ito & Martel, 2002) have shown. The interaction between previous and subsequent intrusions has been suggested as a driving factor in controlling dike trajectories (e.g. Kühn & Dahm, 2008) or recurring dike patterns (e.g. Takada, 1997), and dictating the architecture of reservoirs formed by discrete intrusions (Ferrante et al., 2022), while others have stressed the importance of the cumulative effect of repeating dikes on the state of stress at volcanoes (e.g. Cayol & Cornet, 1998).

All these stress sources can be integrated in our models as they stand now. Including stress mechanisms that are not well-constrained, however, ultimately adds more uncertainty to a model rather than improve it. Thus, in a real scenario, it is more beneficial to include only the stress sources that are most relevant and well-known.

In our scenarios, dike pathways must stop at a given MDT before reaching the surface (See Section 2.2). The MDT we set is compatible with the distance at which dike interaction with the free surface becomes significant (Pollard & Holzhausen, 1979). Surface deformation induced by the incoming dike may cause graben faulting to occur (e.g. Hjartardóttir et al., 2016; Xu et al., 2016), thereby relaxing stresses and inducing the dike to stop before reaching the surface. This aspect is important, and may be included in future models.

Many dikes in our tests stop before reaching the surface. This happens in both models when the interplay between the buoyancy force and the external stress gradients is no longer sufficient to drive the dike upward, and is often associated to gravitational loading (topographic highs). This is shown specifically in Figure 3b, where TIM and SAM dikes stop and spread laterally beneath a topographic load. In scenarios STC-6,7 we also notice how dikes ascending below steep hills often stop before reaching the MDT. Analog models (e.g. fluid-filled cracks propagating in gelatin, as in Kervyn et al., 2009), may further validate such conclusions. Dikes stopping in the subsurface are generally coherent with the fact that most diking episodes do not lead to eruptions (e.g. Gudmundsson, 1983, 1995), although more mechanisms that may stop dikes have been proposed than those that we model here, such as mechanical layering of host rock (Gudmundsson & Brenner, 2004; Geshi et al., 2012) and dike-fault interaction (Maccaferri et al., 2016). In further tests not reported here, SAM dikes with lower magma density (i.e. higher buoyancy) overcame such stress barriers, in accordance with previous models by Dahm (2000a); Maccaferri et al. (2011).

The outcomes of our synthetic scenarios, from the simplest to the more complex, show that dikes are deflected away from topographic lows (calderas), and attracted by topographic highs (hills, resurgent domes), even short-wavelength ones (e.g. a 5 km wide resurgent dome in STC-8). This is consistent with previous dike propagation and stress models considering topographic loading/unloading (Dahm, 2000a; Roman & Jaupart, 2014; Corbi et al., 2016; Rivalta et al., 2019) and with results from gelatin-based analog models (Gaete et al., 2019; Mantiloni et al., 2021). Comparison to natural settings requires further discussion. The few synthetic scenarios we present here are not designed to reproduce the wide variety of vent patterns observed at real calderas. They do, nonetheless, reproduce some common features of vent distribution in calderas. Scenarios STC-2 and STC-4,5,6,7 involve calderas lying on a coastline, with most or all dikes ending up on the mainland. This is compatible with vent patterns in similar worldwide settings, such as Campi Flegrei (Smith et al., 2011). In our tests, no dike trajectories end up within the caldera, except in STC-6 and STC-8. Among worldwide calderas, we find several examples where past eruptive vents lie predominantly at or outside the caldera rim, as our model suggests: for instance, Alcedo, Cerro Azul, Darwin, Fernandina, Sierra Negra and Wolf calderas, Galápagos (Chadwick & Howard, 1991), or Aira caldera, Japan, (Geshi et al., 2020). Still, vents opening within a caldera can be observed in several other settings, like Newberry caldera, Oregon (MacLeod et al., 1982), Santorini caldera, Greece (Sigurdsson et al., 2006), or Campi Flegrei caldera, Italy (Smith et al., 2011). Intracaldera vent openings are predicted when the unloading pressure of the caldera is low or reduced by refilling (STC-6), or if large extensional tectonic stresses or resurgent domes are present (STC-8). Nonetheless, these three factors are not always associated with intracaldera vents in nature (e.g. no eruptions have occurred at Long Valley caldera's resurgent dome after doming inception, Hildreth, 2004). Applying a model to a real caldera entails a deeper understanding of its evolution, stratigraphy and eruptive history, and requires dedicated work. For this reason, we chose not to apply our models to real calderas in this work, as running our model for a real scenario without a proper calibration of the stress state is no different than setting up a synthetic scenario with arbitrary stress. We remark, however, that the fast dike propagation model we presented here is particularly suited for stress calibration procedures, such as the one by (Rivalta et al., 2019). This will be the subject of a future work.

Our model does not consider the viscous flow of magma within dikes and, as such, does not model dike velocity. The pathways predicted by our model, however, may be combined with existing models of dike velocity to integrate the two approaches (e.g. Pinel et al., 2017; Pansino et al., 2022).

In conclusion, we have developed a fast and flexible dike propagation model, that may complement the numerical model by Davis et al. (2020, 2021) over different appli-

cations. The outcomes of our synthetic scenarios are also consistent with observations at many real calderas. Stress models, however, are still critical and not yet fully understood. In a real-case application, our scenarios would be the end point of a stress calibration, whereby the stress state of a volcanic region is constrained through a statistical procedure aiming at matching dike simulations with observations, such as past vent locations (Rivalta et al., 2019), orientation of exposed dikes (Maerten et al., 2022) or focal mechanisms (Zhan et al., 2022). Our model is well-suited for such purpose. Once the stress is calibrated, it may be used to perform a long-term forecast on future vent locations, while the more sophisticated model may be employed to produce short-term propagation scenarios for incipient dike intrusions.

Acknowledgments

We are grateful to Kyle Anderson, Torsten Dahm, Francesco Maccaferri, Mehdi Nikkhoo and Virginie Pinel for constructive discussion and suggestions. L.M. is funded by the DFG grant N. RI 2782/6-1—ZO 277/3-1 within the MagmaPropagator project.

Data availability statement: the open-source Boundary-Element tool *Cut&Displace* is found at https://doi.org/10.5281/zenodo.3694164. The open-source Julia code used for TIM is found at https://doi.org/10.5281/zenodo.4726796 and https://doi.org/10.5281/zenodo.4727208. The code for SAM and the data of the synthetic scenarios are available at *an open-access link to a Zenodo archive will be provided*.

References

Anderson, E. M. (1937). Ix.—the dynamics of the formation of cone-sheets, ring-dykes, and caldron-subsidences. *Proceedings of the Royal Society of Edinburgh*, *56*, 128–157.

Bagnardi, M., Amelung, F., & Poland, M. P. (2013). A new model for the growth of basaltic shields based on deformation of fernandina volcano, galápagos islands. *Earth and Planetary Science Letters*, *377*, 358–366.

Branca, S., Carbone, D., & Greco, F. (2003). Intrusive mechanism of the 2002 ne-rift eruption at mt. etna (italy) inferred through continuous microgravity data and volcanological evidences. *Geophysical Research Letters*, *30*(20).

Cayol, V., & Cornet, F. H. (1998). Three-dimensional modeling of the 1983–1984 eruption at piton de la fournaise volcano, réunion island. *Journal of Geophysical Research: Solid Earth*, *103*(B8), 18025–18037.

Cesca, S., Letort, J., Razafindrakoto, H. N., Heimann, S., Rivalta, E., Isken, M. P., ... others (2020). Drainage of a deep magma reservoir near mayotte inferred from seismicity and deformation. *Nature Geoscience*, *13*(1), 87–93.

Chadwick, W. W., & Dieterich, J. H. (1995). Mechanical modeling of circumferential and radial dike intrusion on galapagos volcanoes. *Journal of Volcanology and Geothermal Research*, *66*(1-4), 37–52.

Chadwick, W. W., & Howard, K. A. (1991). The pattern of circumferential and radial eruptive fissures on the volcanoes of fernandina and isabela islands, galapagos. *Bulletin of Volcanology*, *53*(4), 259–275.

Corbi, F., Rivalta, E., Pinel, V., Maccaferri, F., & Acocella, V. (2016). Understanding the link between circumferential dikes and eruptive fissures around calderas based on numerical and analog models. *Geophysical Research Letters*, *43*(12), 6212–6219.

Corbi, F., Rivalta, E., Pinel, V., Maccaferri, F., Bagnardi, M., & Acocella, V. (2015). How caldera collapse shapes the shallow emplacement and transfer of magma in active volcanoes. *Earth and Planetary Science Letters*, *431*, 287–293.

Crouch, S. L., Starfield, A. M., & Rizzo, F. (1983). Boundary element methods in solid mechanics.

Dahm, T. (2000a). Numerical simulations of the propagation path and the arrest of fluid-filled fractures in the earth. *Geophysical Journal International*, *141*(3), 623–638. doi: 10.1046/j.1365-246x.2000.00102.x

Dahm, T. (2000b). On the shape and velocity of fluid-filled fractures in the earth. *Geophysical Journal International*, *142*(1), 181–192.

Davis, T., Bagnardi, M., Lundgren, P., & Rivalta, E. (2021). Extreme curvature of shallow magma pathways controlled by competing stresses: insights from the 2018 sierra negra eruption. *Geophysical Research Letters*, *48*(13), e2021GL093038.

Davis, T., Healy, D., Bubeck, A., & Walker, R. (2017). Stress concentrations around voids in three dimensions: The roots of failure. *Journal of Structural Geology*, *102*, 193–207. doi: 10.1016/j.jsg.2017.07.013

Davis, T., Healy, D., & Rivalta, E. (2019). Slip on wavy frictional faults: Is the 3rd dimension a sticking point? *Journal of Structural Geology*, *119*, 33–49. doi: 10.1016/j.jsg.2018.11.009

Davis, T., Rivalta, E., & Dahm, T. (2020). Critical fluid injection volumes for uncontrolled fracture ascent. *Geophysical Research Letters*, e2020GL087774. doi: 10.1029/2020GL087774

Dieterich, J. H. (1988). Growth and persistence of hawaiian volcanic rift zones. *Journal of Geophysical Research: Solid Earth*, *93*(B5), 4258–4270.

Dumont, Q., Cayol, V., Froger, J.-L., & Peltier, A. (2022). 22 years of satellite imagery reveal a major destabilization structure at piton de la fournaise. *Nature Communications*, *13*(1), 1–11.

Ebinger, C., Ayele, A., Keir, D., Rowland, J., Yirgu, G., Wright, T., ... Hamling, I. (2010). Length and timescales of rift faulting and magma intrusion: The afar rifting cycle from 2005 to present. *Annual Review of Earth and Planetary Sciences*, *38*(1), 439–466.

Einarsson, P., Brandsdottir, B., et al. (1980). Seismological evidence for lateral magma intrusion during the july 1978 deflation of the krafla volcano in ne-iceland. *Journal of Geophysics*, *47*(1), 160–165.

Ferrante, G., Rivalta, E., & Maccaferri, F. (2022). Numerical simulation of magma pathways and vent distribution in rifts from the early stages to maturity.

Gaete, A., Kavanagh, J. L., Rivalta, E., Hazim, S. H., Walter, T. R., & Dennis, D. J. (2019). The impact of unloading stresses on post-caldera magma intrusions. *Earth and Planetary Science Letters*, *508*, 109–121. doi: 10.1016/j.epsl.2018.12.016

Geshi, N., Kusumoto, S., & Gudmundsson, A. (2012). Effects of mechanical layering of host rocks on dike growth and arrest. *Journal of Volcanology and Geothermal Research*, *223*, 74–82.

Geshi, N., Yamada, I., Matsumoto, K., Nishihara, A., & Miyagi, I. (2020). Accumulation of rhyolite magma and triggers for a caldera-forming eruption of the aira caldera, japan. *Bulletin of Volcanology*, *82*(6), 1–18.

Gómez-Vasconcelos, M. G., Villamor, P., Cronin, S. J., Palmer, A., Procter, J., & Stewart, R. B. (2020). Spatio-temporal associations between dike intrusions and fault ruptures in the tongariro volcanic center, new zealand. *Journal of Volcanology and Geothermal Research*, *404*, 107037.

Grosfils, E. B., McGovern, P. J., Gregg, P. M., Galgana, G. A., Hurwitz, D. M., Long, S. M., & Chestler, S. R. (2015). Elastic models of magma reservoir mechanics: a key tool for investigating planetary volcanism. *Geological Society, London, Special Publications*, *401*(1), 239–267.

Gudmundsson, A. (1983). Form and dimensions of dykes in eastern iceland. *Tectonophysics*, *95*(3-4), 295–307.

Gudmundsson, A. (1995). Infrastructure and mechanics of volcanic systems in iceland. *Journal of Volcanology and Geothermal Research*, *64*(1-2), 1–22.

Gudmundsson, A. (2002). Emplacement and arrest of sheets and dykes in cen-

tral volcanoes. *Journal of Volcanology and Geothermal Research*, *116*(3-4), 279–298.

Gudmundsson, A. (2006). How local stresses control magma-chamber ruptures, dyke injections, and eruptions in composite volcanoes. *Earth-science reviews*, *79*(1-2), 1–31.

Gudmundsson, A., & Brenner, S. L. (2004). How mechanical layering affects local stresses, unrests, and eruptions of volcanoes. *Geophysical Research Letters*, *31*(16).

Heimisson, E. R., Hooper, A., & Sigmundsson, F. (2015). Forecasting the path of a laterally propagating dike. *Journal of Geophysical Research: Solid Earth*, *120*(12), 8774–8792.

Hildreth, W. (2004). Volcanological perspectives on long valley, mammoth mountain, and mono craters: several contiguous but discrete systems. *Journal of Volcanology and Geothermal Research*, *136*(3-4), 169–198.

Hildreth, W., Fierstein, J., & Calvert, A. (2017). Early postcaldera rhyolite and structural resurgence at long valley caldera, california. *Journal of Volcanology and Geothermal Research*, *335*, 1–34.

Hjartardóttir, Á. R., Einarsson, P., Gudmundsson, M. T., & Högnadóttir, T. (2016). Fracture movements and graben subsidence during the 2014 bárarbunga dike intrusion in iceland. *Journal of Volcanology and Geothermal Research*, *310*, 242–252.

Ito, G., & Martel, S. J. (2002). Focusing of magma in the upper mantle through dike interaction. *Journal of Geophysical Research: Solid Earth*, *107*(B10), ECV–6.

Jaeger, J., Cook, N., & Zimmermann, R. (2007). Fundamentals of rock mechanics. blackwell, oxford.

Kervyn, M., Ernst, G., van Wyk de Vries, B., Mathieu, L., & Jacobs, P. (2009). Volcano load control on dyke propagation and vent distribution: Insights from analogue modeling. *Journal of Geophysical Research: Solid Earth*, *114*(B3).

Kühn, D., & Dahm, T. (2008). Numerical modelling of dyke interaction and its influence on oceanic crust formation. *Tectonophysics*, *447*(1-4), 53–65.

Le Corvec, N., Menand, T., & Lindsay, J. (2013). Interaction of ascending magma with pre-existing crustal fractures in monogenetic basaltic volcanism: an experimental approach. *Journal of Geophysical Research: Solid Earth*, *118*(3), 968–984.

Maccaferri, F., Bonafede, M., & Rivalta, E. (2010). A numerical model of dyke propagation in layered elastic media. *Geophysical Journal International*, *180*(3), 1107–1123. doi: 10.1111/j.1365-246X.2009.04495.x

Maccaferri, F., Bonafede, M., & Rivalta, E. (2011). A quantitative study of the mechanisms governing dike propagation, dike arrest and sill formation. *Journal of Volcanology and Geothermal Research*, *208*(1-2), 39–50. doi: 10.1016/j.jvolgeores.2011.09.001

Maccaferri, F., Richter, N., & Walter, T. R. (2017). The effect of giant lateral collapses on magma pathways and the location of volcanism. *Nature communications*, *8*(1), 1–11.

Maccaferri, F., Rivalta, E., Keir, D., & Acocella, V. (2014). Off-rift volcanism in rift zones determined by crustal unloading. *Nature Geoscience*, *7*(4), 297–300. doi: 10.1038/ngeo2110

Maccaferri, F., Rivalta, E., Passarelli, L., & Aoki, Y. (2016). On the mechanisms governing dike arrest: Insight from the 2000 miyakejima dike injection. *Earth and Planetary Science Letters*, *434*, 64–74.

MacLeod, N. S., Sherrod, D. R., Chitwood, L. A., & Jensen, R. A. (1982). *Geologic map of newberry volcano, deschutes, klamath, and lake counties, oregon.* Geological Survey.

Maerten, F., Maerten, L., Plateaux, R., & Cornard, P. (2022). *Joint inversion*

of tectonic stress and magma pressures using dyke trajectories (Tech. Rep.). Copernicus Meetings.

Mantiloni, L., Davis, T., Gaete Rojas, A. B., & Rivalta, E. (2021). Stress inversion in a gelatin box: testing eruptive vent location forecasts with analog models. *Geophysical Research Letters*, *48*(6).

Martel, S. J., & Muller, J. R. (2000). A two-dimensional boundary element method for calculating elastic gravitational stresses in slopes. *Pure and Applied Geophysics*, *157*(6-8), 989–1007. doi: 10.1007/s000240050014

Martí, J., Becerril, L., & Rodríguez, A. (2022). How long-term hazard assessment may help to anticipate volcanic eruptions: The case of la palma eruption 2021 (canary islands). *Journal of Volcanology and Geothermal Research*, 107669.

McGarr, A., & Gay, N. (1978). State of stress in the earth's crust. *Annual Review of Earth and Planetary Sciences*, *6*(1), 405–436.

McGuire, W., & Pullen, A. (1989). Location and orientation of eruptive fissures and feederdykes at mount etna; influence of gravitational and regional tectonic stress regimes. *Journal of Volcanology and Geothermal Research*, *38*(3-4), 325–344.

McKenzie, D. (1978). Some remarks on the development of sedimentary basins. *Earth and Planetary science letters*, *40*(1), 25–32.

McTigue, D. F., & Mei, C. C. (1981). Gravity-induced stresses near topography of small slope. *Journal of Geophysical Research: Solid Earth*, *86*(B10), 9268–9278.

McTigue, D. F., & Mei, C. C. (1987). Gravity-induced stresses near axisymmetric topography of small slope. *International Journal for Numerical and Analytical Methods in Geomechanics*, *11*(3), 257–268.

Müller, B., Zoback, M. L., Fuchs, K., Mastin, L., Gregersen, S., Pavoni, N., ... Ljunggren, C. (1992). Regional patterns of tectonic stress in europe. *Journal of Geophysical Research: Solid Earth*, *97*(B8), 11783–11803.

Muller, J. R., Ito, G., & Martel, S. J. (2001). Effects of volcano loading on dike propagation in an elastic half-space. *Journal of Geophysical Research: Solid Earth*, *106*(B6), 11101–11113. doi: 10.1029/2000JB900461

Muller, O. H., & Pollard, D. D. (1977). The stress state near spanish peaks, colorado determined from a dike pattern. *Pure and Applied Geophysics*, *115*(1-2), 69–86.

Nakada, S., Nagai, M., Kaneko, T., Nozawa, A., & Suzuki-Kamata, K. (2005). Chronology and products of the 2000 eruption of miyakejima volcano, japan. *Bulletin of Volcanology*, *67*(3), 205–218.

Neri, M., Rivalta, E., Maccaferri, F., Acocella, V., & Cirrincione, R. (2018). Etnean and hyblean volcanism shifted away from the malta escarpment by crustal stresses. *Earth and Planetary Science Letters*, *486*, 15–22.

Nikkhoo, M., & Walter, T. R. (2015). Triangular dislocation: an analytical, artefact-free solution. *Geophysical Journal International*, *201*(2), 1119–1141.

Orsi, G., De Vita, S., & Di Vito, M. (1996). The restless, resurgent campi flegrei nested caldera (italy): constraints on its evolution and configuration. *Journal of Volcanology and Geothermal Research*, *74*(3-4), 179–214.

Pansino, S., Emadzadeh, A., & Taisne, B. (2022). Modeling dike propagation in both vertical length and horizontal breadth. *Journal of Geophysical Research: Solid Earth*, e2022JB024593.

Pansino, S., & Taisne, B. (2019). How magmatic storage regions attract and repel propagating dikes. *Journal of Geophysical Research: Solid Earth*, *124*(1), 274–290.

Patrick, M. R., Houghton, B. F., Anderson, K. R., Poland, M. P., Montgomery-Brown, E., Johanson, I., ... Elias, T. (2020). The cascading origin of the 2018 kīlauea eruption and implications for future forecasting. *Nature Communications*, *11*(1), 1–13.

Pinel, V., Carrara, A., Maccaferri, F., Rivalta, E., & Corbi, F. (2017). A two-step model for dynamical dike propagation in two dimensions: Application to the july 2001 etna eruption. *Journal of Geophysical Research: Solid Earth*, *122*(2), 1107–1125.

Pollard, D. D. (1987). Elementary fracture mechanics applied to the structural interpretation of dykes. In *Mafic dyke swarms* (Vol. 34, pp. 5–24).

Pollard, D. D., Fletcher, R. C., et al. (2005). *Fundamentals of structural geology.* Cambridge University Press.

Pollard, D. D., & Holzhausen, G. (1979). On the mechanical interaction between a fluid-filled fracture and the earth's surface. *Tectonophysics*, *53*(1-2), 27–57.

Rivalta, E., Corbi, F., Passarelli, L., Acocella, V., Davis, T., & Di Vito, M. A. (2019). Stress inversions to forecast magma pathways and eruptive vent location. *Science advances*, *5*(7), eaau9784. doi: 10.1126/sciadv.aau9784

Rivalta, E., Taisne, B., Bunger, A., & Katz, R. (2015). A review of mechanical models of dike propagation: Schools of thought, results and future directions. *Tectonophysics*, *638*, 1–42.

Roman, A., & Jaupart, C. (2014). The impact of a volcanic edifice on intrusive and eruptive activity. *Earth and Planetary Science Letters*, *408*, 1–8. doi: 10.1016/j.epsl.2014.09.016

Rubin, A. M. (1995). Propagation of magma-filled cracks. *Annual Review of Earth and Planetary Sciences*, *23*(1), 287–336.

Rubin, A. M., & Gillard, D. (1998). Dike-induced earthquakes: Theoretical considerations. *Journal of Geophysical Research: Solid Earth*, *103*(B5), 10017–10030.

Savage, W., Swolfs, H., & Amadei, B. (1992). On the state of stress in the near-surface of the earth's crust. *Pure and Applied Geophysics*, *138*(2), 207–228.

Savage, W., Swolfs, H., & Powers, P. (1985). Gravitational stresses in long symmetric ridges and valleys. In *International journal of rock mechanics and mining sciences & geomechanics abstracts* (Vol. 22, pp. 291–302).

Secor Jr, D. T., & Pollard, D. D. (1975). On the stability of open hydraulic fractures in the earth's crust. *Geophysical Research Letters*, *2*(11), 510–513.

Sigmundsson, F., Hooper, A., Hreinsdóttir, S., Vogfjörd, K. S., Ófeigsson, B. G., Heimisson, E. R., ... others (2015). Segmented lateral dyke growth in a rifting event at bárarbunga volcanic system, iceland. *Nature*, *517*(7533), 191–195.

Sigurdsson, H., Carey, S., Alexandri, M., Vougioukalakis, G., Croff, K., Roman, C., ... others (2006). Marine investigations of greece's santorini volcanic field. *Eos, Transactions American Geophysical Union*, *87*(34), 337–342.

Slim, M., Perron, J. T., Martel, S. J., & Singha, K. (2015). Topographic stress and rock fracture: A two-dimensional numerical model for arbitrary topography and preliminary comparison with borehole observations. *Earth Surface Processes and Landforms*, *40*(4), 512–529.

Smith, V., Isaia, R., & Pearce, N. (2011). Tephrostratigraphy and glass compositions of post-15 kyr campi flegrei eruptions: implications for eruption history and chronostratigraphic markers. *Quaternary Science Reviews*, *30*(25-26), 3638–3660.

Smittarello, D., Smets, B., Barrière, J., Michellier, C., Oth, A., Shreve, T., ... others (2022). Precursor-free eruption triggered by edifice rupture at nyiragongo volcano. *Nature*, *609*(7925), 83–88.

Stephansson, O. (1988). Ridge push and glacial rebound as rock stress generators in fennoscandia. *Bulletin of the Geological Institutions of the University of Uppsala*, *14*, 39–48.

Tada, H., Paris, P., & Irwin, G. (2000). *American society of mechanical engineers., asm international., the stress analysis of cracks handbook.* ASME Press: Professional Engineering Pub.: ASM International, New York.

Taisne, B., Tait, S., & Jaupart, C. (2011). Conditions for the arrest of a vertical propagating dyke. *Bulletin of Volcanology*, *73*(2), 191–204.

Takada, A. (1997). Cyclic flank-vent and central-vent eruption patterns. *Bulletin of volcanology*, *58*(7), 539–556.

Townsend, M. R., Pollard, D. D., & Smith, R. P. (2017). Mechanical models for dikes: A third school of thought. *Tectonophysics*, *703*, 98–118.

Uhira, K., Baba, T., Mori, H., Katayama, H., & Hamada, N. (2005). Earthquake swarms preceding the 2000 eruption of miyakejima volcano, japan. *Bulletin of Volcanology*, *67*(3), 219–230.

Urbani, S., Acocella, V., Rivalta, E., & Corbi, F. (2017). Propagation and arrest of dikes under topography: Models applied to the 2014 bardarbunga (iceland) rifting event. *Geophysical Research Letters*, *44*(13), 6692–6701.

Ventura, G., Vilardo, G., & Bruno, P. P. (1999). The role of flank failure in modifying the shallow plumbing system of volcanoes: an example from somma-vesuvius, italy. *Geophysical Research Letters*, *26*(24), 3681–3684.

Walter, T. R., Troll, V. R., Cailleau, B., Belousov, A., Schmincke, H.-U., Amelung, F., et al. (2005). Rift zone reorganization through flank instability in ocean island volcanoes: an example from tenerife, canary islands. *Bulletin of Volcanology*, *67*(4), 281–291.

Weertman, J. (1971). Theory of water-filled crevasses in glaciers applied to vertical magma transport beneath oceanic ridges. *Journal of Geophysical Research*, *76*(5), 1171–1183.

Wright, T. J., Sigmundsson, F., Pagli, C., Belachew, M., Hamling, I. J., Brandsdóttir, B., ... others (2012). Geophysical constraints on the dynamics of spreading centres from rifting episodes on land. *Nature Geoscience*, *5*(4), 242–250.

Xu, W., & Jónsson, S. (2014). The 2007–8 volcanic eruption on jebel at tair island (red sea) observed by satellite radar and optical images. *Bulletin of Volcanology*, *76*(2), 1–14.

Xu, W., Jónsson, S., Corbi, F., & Rivalta, E. (2016). Graben formation and dike arrest during the 2009 harrat lunayyir dike intrusion in saudi arabia: Insights from insar, stress calculations and analog experiments. *Journal of Geophysical Research: Solid Earth*, *121*(4), 2837–2851.

Zhan, Y., Roman, D. C., Le Mével, H., & Power, J. A. (2022). Earthquakes indicated stress field change during the 2006 unrest of augustine volcano, alaska. *Geophysical Research Letters*, e2022GL097958.

Ziv, A., Rubin, A. M., & Agnon, A. (2000). Stability of dike intrusion along preexisting fractures. *Journal of Geophysical Research: Solid Earth*, *105*(B3), 5947–5961.